science.sciencemag.org/content/366/6469/1125/suppl/DC1

Supplementary Material for

Magnetization switching by magnon-mediated spin torque through an antiferromagnetic insulator

Yi Wang, Dapeng Zhu, Yumeng Yang, Kyusup Lee, Rahul Mishra, Gyungchoon Go, Se-Hyeok Oh, Dong-Hyun Kim, Kaiming Cai, Enlong Liu, Shawn D. Pollard, Shuyuan Shi, Jongmin Lee, Kie Leong Teo, Yihong Wu, Kyung-Jin Lee, Hyunsoo Yang*

*Corresponding author. Email: eleyang@nus.edu.sg

Published 29 November 2019, *Science* **366**, 1125 (2019)
DOI: 10.1126/science.aav8076

This PDF file includes:

Materials and Methods

Sample preparations. High quality 8-nm topological insulator Bi_2Se_3 films are grown on c-plane sapphire substrates by a molecular beam epitaxy (MBE) system with a base pressure < 1.5×10^{-9} Torr. First, the sapphire substrate is cleaned in acetone, isopropanol, and de-ionized water, and subsequently transferred into the growth chamber and annealed at 750 °C for 30 min in a vacuum. For the Bi_2Se_3 deposition, elemental Bi (6N) and Se (5N) solid sources are evaporated from standard Knudsen cells under a Se/Bi flux ratio of ~20. To reduce the Se vacancies in Bi_2Se_3, initial 2–3 quintuple layer (QL) Bi_2Se_3 is deposited at 150 °C, and then the substrate temperature is ramped to 250 °C at 5 °C/min under Se flux for the second step growth. The antiferromagnetic insulator NiO (t_{NiO} = 0 – 30 nm) and ferromagnetic metal NiFe (Py, 6 nm) are deposited onto the Bi_2Se_3 films using radio frequency (RF) and direct current sputtering, respectively, with a base pressure of 3×10^{-9} Torr at room temperature. An in-situ magnetic field ~ 550 Oe is applied to induce a uniaxial in-plane magnetic anisotropy in the Py layer. Finally, the stacks are protected by the sputtered MgO (1 nm)/SiO_2 (4 nm) layer. It is confirmed that the NiO layer is insulating by the Van der Pauw method.

For the spin torque ferromagnetic resonance (ST-FMR) devices, the films are patterned into rectangular-shaped microstrips by photolithography and ion milling. The current channel width is 15 μm. Then, coplanar waveguides (CPW) are fabricated. The device impedance is ~50 Ω. For the switching devices, an isolated Py (6 nm), $Co_{40}Fe_{40}B_{20}$ (3 nm) or Cu (6 nm)/Py (6 nm) rectangle is patterned on top of the NiO layer by photolithography and ion milling as shown in Fig. 4A. Then a 6-nm SiO_2 layer is deposited to protect against oxidization.

ST-FMR measurements. The ST-FMR signal, V_{mix}, is produced across the ST-FMR device by the rectification of anisotropic magnetoresistance oscillating at the same frequency as a RF current I_{RF} (*28*). The frequencies and nominal power of I_{RF} are 8–10 GHz and 13 dBm, respectively. I_{RF} is amplitude-modulated by a low frequency sinusoidal wave signal with a frequency of 256.5 Hz. An in-plane external magnetic field (H) is applied at a fixed angle at θ_H = 35° with respect to I_{RF} direction. Finally, V_{mix} is detected by a lock-in amplifier. The amplitude of symmetric component (V_S) can be determined from the fits of ST-FMR signals as shown in Fig. 3B, which is correlated with the damping-like torque, τ_{DL}. Consequently, the spin torque ratio θ_i is evaluated using $V_S = -\frac{I_{RF}\gamma \cos\theta_H}{4}\frac{dR}{d\theta_H}\tau_{DL}\frac{1}{\Delta}F_S(H)$, $\sigma_i = \tau_{DL}M_s t_{Py}/E$ and $\theta_i = J_i/J_C = \sigma_i/\sigma$ (*17, 27*), where γ is the gyromagnetic ratio, $dR/d\theta_H$ is the angle-dependent magnetoresistance at θ_H, Δ is the linewidth of ST-FMR signal in the frequency domain, $F_S(H)$ is a symmetric Lorentzian, M_s is the saturation magnetization of Py, t_{Py} is the thickness of Py, σ is the Bi_2Se_3 conductivity, E is the microwave field across the device, J_C is the charge current density in the Bi_2Se_3 layer, σ_i, J_i *and* θ_i are the spin conductivity, spin current and spin torque ratio, respectively. Here the subscript 'i' means that it is either due to the electrical spin current J_S (i = S) or the magnon current J_M (i = M).

Switching measurements. We first initialize the magnetization of the isolated Py rectangle along the +y or –y-axis (see Fig. 4, B, C and E) with an in-plane external magnetic field H. We then remove H and apply a pulsed current I (pulse width of 30 μs) to observe the magnetization switching using a longitudinal magneto-optic Kerr effect (MOKE) microscope. The Py magnetization shows an in-plane easy axis along the y-axis (i.e. perpendicular to I). The MOKE images are captured after I is off, so that there is no current induced spurious effects in the MOKE images. The same measurement procedures are followed for $Co_{40}Fe_{40}B_{20}$ magnetization switching measurements.

Supplementary Text

Section 1. Atomic-force microscopy (AFM) images of Bi_2Se_3 and Bi_2Se_3/NiO films

As shown in Fig. S1A, the Bi_2Se_3 films have smooth surface with a roughness of ~0.59 nm and show a clear terrace step of 1 quintuple layer (~1 nm). The morphology indicates the high quality of Bi_2Se_3 films. As we deposit 5-nm NiO (Fig. S1B) and 25-nm NiO (Fig. S1C) on top of Bi_2Se_3, we find the films still show smooth surfaces with a roughness of ~ 0.61 nm (Bi_2Se_3 8 nm/NiO 5 nm, Fig. S1B) and 0.64 nm (Bi_2Se_3 8 nm/NiO 25 nm, Fig. S1C). Moreover, the morphology of the triangles and terrace steps can still be observed with the NiO layer, indicating that the surface of the Bi_2Se_3 films are intact. Some small island structures can be seen on the film surface in Fig. S1C, which might be due to polycrystal NiO grains in the thick NiO films.

Section 2. NiO/Py interface contribution to spin torque ratio θ_t

Recent studies (*41-43*) have found that ferromagnet/oxide interfaces could generate a spin-orbit torque. Figure S2A shows the raw θ_t data, obtained from the ST-FMR measurements, without correcting the interface contribution. In our Bi_2Se_3 (8 nm)/NiO (t_{NiO} = 0–100 nm)/NiFe (Py, 6 nm) ST-FMR devices, I_{RF} flows not only through the Bi_2Se_3 layer (current density J_C) but also through the Py layer ($J_{C\text{-}Py}$) and the NiO/Py interface ($J_{C\text{-}int}$) (see schematic in Fig. S2B). In order to evaluate the pure magnon-torque effect, we need to measure the NiO/Py interface contribution θ_{int}.

We evaluate θ_{int} at the NiO/Py interface using the established 2nd harmonic measurements (*44-46*) in the Si/SiO_2 sub./NiO (t_{NiO})/Py (6 nm) control samples (Fig. S2C). The patterned Hall bar has a 4-μm wide channel width. An alternating current (AC) with an amplitude of 4 mA is applied into the device with a frequency of 317.3 Hz. An external magnetic field H is rotating in the Hall bar plane with an azimuthal angle φ. The Py magnetization is oscillating around H due to the

damping-like torque (τ_{DL}) and field-like torque (τ_{FL}) including the Oersted field torque induced by the current. The 1st harmonic (i.e. planar Hall signal) and 2nd harmonic Hall voltages are recorded using lock-in amplifiers at different H. The 1st and 2nd harmonic transverse resistances can be written as (*44-46*)

$$R_{xy}^{\omega} = R_P \sin 2\varphi, \tag{S1}$$

$$R_{xy}^{2\omega} = (R_{DL}^{2\omega} + R_{ANE}^{2\omega})\cos\varphi + R_{FL}^{2\omega}\cos\varphi\cos 2\varphi, \tag{S2}$$

where R_P is the planar Hall resistance. $R_{DL}^{2\omega} = H_{DL}R_A/2(H - H_{deg} - H_{ani})$ is correlated with τ_{DL}, where R_A is the anomalous Hall resistance, H_{DL} is the damping-like torque induced effective field at the NiO/Py interface, H_{deg} and H_{ani} are respectively the out of plane demagnetization field and in-plane anisotropy field of the Py layer. $R_{ANE}^{2\omega}$ is due to the anomalous Nernst effect (ANE) induced by the thermal gradient normal to the film plane, which is almost constant at each H. $R_{FL}^{2\omega} = -H_{FL}R_P/H$ is correlated with the field-like torque including the Oersted field torque, where H_{FL} is the field-like torque induced effective field. We obtain the values of θ_{int} using $\theta_{int} = H_{DL}\frac{2e}{\hbar}\frac{M_s t_{Py}}{J_{C\text{-}int}}$, where the $J_{C\text{-}int}$ is the charge current density at the NiO/Py interface and we assume it is the same as the current density in the Py layer.

Figure S2D shows R_{xy}^{ω} as a function of φ measured at a representative H = 500 Oe. It is fitted by Eq. (S1), indicating that the Py magnetization always follows the H direction. Figure S2E shows $R_{xy}^{2\omega}$ as a function of φ measured at the same H. We find that it is well fitted with Eq. (S2). By following the analysis procedures in previous reports (*44-46*), we obtain $R_{DL}^{2\omega}$ and thus H_{DL} values by substracting the $R_{ANE}^{2\omega}$ term, which is the determined by the intercept of the y-axis (Fig. S2F). Moreover, the $R_{FL}^{2\omega}$ data converge towards zero (Fig. S2G), which is in line with the expected

behavior of $R_{FL}^{2\omega}$ being inversely proportional to H. Finally, we determine θ_{int} at the NiO/Py interface at different t_{NiO} (Fig. S2H). We find that θ_{int} remains almost constant at ~ 0.011 for t_{NiO} ≥ 5 nm, with the same sign as that in Bi_2Se_3 or Pt (*27, 47*).

We then obtain the t_{NiO}-dependent spin torque ratio by excluding the contribution of the NiO/Py interface (i.e. θ_{int}) at room temperature, which is shown in Fig. 3C of the main text. Since the θ_{int} remains almost constant as $t_{NiO} \geq 5$ nm, we assume that θ_{int} has a constant value up to t_{NiO} = 100 nm. In Bi_2Se_3 (8 nm)/NiO (t_{NiO} = 0–100 nm)/Py (6 nm) devices, the total flow of the spin angular momentum ($J_{S\text{-}total}$) into the Py layer in each device can be calculated by $J_{S\text{-}total} = \frac{2e}{\hbar}\tau_{DL} M_s t_{Py}$, where the damping-like torque τ_{DL} is determined from the ST-FMR measurements. As shown in Fig. S2B, $J_{S\text{-}total} = J_i + J_{S\text{-}int}$. The $J_{S\text{-}int} = \theta_{int} J_{C\text{-}int}$ and $J_i = \theta_i J_C$ are the spin current density from the NiO/Py interface and spin current density from the Bi_2Se_3/NiO in the device, respectively. Consequently, we obtain θ_i without a NiO/Py interface contribution as a function of t_{NiO} (Fig. 3C).

Section 3. Characterization of magnon current through NiO by THz emission

Recent progresses in optical characterization tools have allowed one to study optically-driven spin current generation in magnetic materials. In particular, a transient spin current driven by an ultrashort optical pulse in a magnetic thin film has been monitored by capturing the electromagnetic wave emitted from a strong spin orbit coupled layer adjacent the magnet based on the inverse spin Hall effect (ISHE). The injected spin current from the magnet into the layer with strong spin-orbit coupling is converted to the charge current, which can generate an electromagnetic wave typically with a terahertz (THz) frequency (*48, 49*). By monitoring the emitted THz wave, one can evaluate the strength of injected spin current (*31, 32*). Therefore, the

THz emission amplitude characterizes the spin-to-charge conversion, which is the reciprocal process of the ST-FMR measurements (charge-to-spin). Specifically, the THz emission amplitude is proportional to the time-averaged transient charge current density J_C converted from spin currents.

In this work, we use a Ti:sapphire regenerative amplifier system operating with a 1 kHz repetition rate, a central wavelength of 800 nm and a pulse duration of 120 fs. The laser beam is divided into two lines; one is used to excite spin currents in the magnetic layer and the other is used to probe the THz emission based on electro-optic sampling. The details of the experiments were reported elsewhere (*50, 51*). Figure S3 shows the THz waveforms emitted from Bi_2Se_3 (8 QL)/NiO (t_{NiO} = 0–100 nm)/Py (6 nm) films. For comparison, the time zero is set to be the temporal peak position and the THz amplitudes are normalized by the control film (t_{NiO} = 0 nm). The in-plane external magnetic field is applied with a strength of 1 kOe, which fully saturates Py magnetization. The sign change of THz waveform (see the inset of Fig. S3) when reversing the magnetic field orientation represents the ISHE-driven THz emission, which is observed in all the films. The THz peak amplitude is extracted for each film with different NiO thicknesses. We find that the NiO thickness dependence of THz amplitude shows almost identical behavior to that measured by ST-FMR (see Fig. 3C). The reproducible NiO thickness dependent behavior from independent THz measurements further validates our observations of magnon torques.

Section 4. Evaluation of spin torque ratio in control devices with MgO insertions

To confirm the magnon torque in our devices, we study the control devices C1 and C2. We have listed the device structures and the spin torque ratios in Table S1. As shown in Table S1, we insert a 6-nm MgO layer at the NiO/NiFe (C1) and Bi_2Se_3/NiO (C2) interfaces. From the ST-FMR measurements, we find that the spin torque ratios θ_i are ~0.09 (C1) and ~0.03 (C2), respectively.

The small θ_l in device C1 indicates that the MgO insulator layer almost blocks the magnon currents through the NiO layer. In device C2, we may keep the property of NiO/Py interface similar to that in device D1 in the main text. The measured spin torque ratio θ_l^* is ~0.13, which can be attributed to the NiO/Py interface contribution. After we subtract the NiO/Py interface contribution as described in section 2, the spin torque ratio θ_l is ~0.03, which is negligibly small compared to that in the device D1 (θ_l ~ 0.3) in the main text. This result further confirms the large magnon torque in our devices.

Section 5. Derivation of the magnon current at the NiO/Py interface

We estimate a transverse magnon current at the NiO/Py interface for the Bi_2Se_3/NiO/Py structure, using a simple drift-diffusion model. A schematic illustration of the model system is shown in Fig. S4. Because the NiO layer is polycrystalline (Fig. 2D), we assume that the magnon propagation in the NiO layer is diffusive. Following Ref. (*36*), the magnon current density in the antiferromagnet is given by

$$\mathbf{J}_{\mathrm{m}}^{\mathrm{AF}} = -\sigma_{\mathrm{m}}^{\mathrm{AF}} \frac{\partial \boldsymbol{\mu}_{\mathrm{m}}^{\mathrm{AF}}}{\partial z}, \tag{S3}$$

where $\sigma_{\mathrm{m}}^{\mathrm{AF}}$ and $\boldsymbol{\mu}_{\mathrm{m}}^{\mathrm{AF}}$ are the magnon conductivity and magnon chemical potential of the antiferromagnetic layer. The vector index stands for the magnon spin polarization direction. Because the magnon chemical potential satisfies the diffusion equation, we have

$$\boldsymbol{\mu}_{\mathrm{m}}^{\mathrm{AF}} = \mathbf{A} e^{z/l_{\mathrm{m}}^{\mathrm{AF}}} + \mathbf{B} e^{-z/l_{\mathrm{m}}^{\mathrm{AF}}}, \tag{S4}$$

where $l_{\mathrm{m}}^{\mathrm{AF}}$ is the magnon diffusion length in the antiferromagnetic layer.

At the Bi_2Se_3/NiO interface, we consider that a constant spin current from Bi_2Se_3 is injected into the NiO layer,

$$\mathbf{J}_{\mathrm{m}}^{\mathrm{AF}}(z = -t_{\mathrm{NiO}}) = \eta \theta J_{\mathrm{C}} \hat{\mathbf{y}}. \tag{S5}$$

where θ is the spin Hall angle of Bi_2Se_3 layer, and is J_C the charge current density in the Bi_2Se_3 layer. η is a parameter which characterizes the angular momentum loss from spin to magnon conversion at the interface. For simplicity, we assume that the magnon dephasing length of a ferromagnet is zero so that the transverse component of the magnon current is absorbed at the interface and exerts a magnon torque on a ferromagnet. The transverse magnon current at the NiO/Py interface is given by (*36*)

$$\mathbf{J}_{\mathrm{m}}^{\perp}(0^{-}) = -\frac{G_{\mathrm{A/F}}^{\perp}}{2\pi}\mathbf{m} \times [\mathbf{m} \times \mu_{\mathrm{m}}^{\mathrm{AF}}(0^{-})], \tag{S6}$$

where $G_{\mathrm{A/F}}^{\perp}$ is the interfacial magnon conductance for the transverse component between NiO and Py and **m** is the magnetization direction of Py. We consider that the magnetization direction in Py layer is $\hat{\mathbf{z}}$. Solving Eqs. (S3)-(S6) with the boundary conditions $J_{\mathrm{m}}^{\mathrm{F}}(z = t_{\mathrm{Py}}) = 0$, we obtain

$$J_x^{\mathrm{m}}(z = 0) = 0, \qquad J_y^{\mathrm{m}}(z = 0) = \eta\theta J_{\mathrm{C}}\,\frac{2G_{\mathrm{A/F}}^{\perp} l_{\mathrm{m}}^{\mathrm{AF}} \kappa_{\mathrm{AF}}}{G_{\mathrm{A/F}}^{\perp} l_{\mathrm{m}}^{\mathrm{AF}}(1+\kappa_{\mathrm{AF}}^2) + 2\pi\sigma_{\mathrm{m}}^{\mathrm{AF}}(1-\kappa_{\mathrm{AF}}^2)}, \tag{S7}$$

where $\kappa_{\mathrm{AF}} = \exp(-t_{\mathrm{NiO}}/l_{\mathrm{m}}^{\mathrm{AF}})$. In Eq. (1) of the main text, $\kappa \equiv \kappa_{\mathrm{AF}}$ and $l_{\mathrm{m}} \equiv l_{\mathrm{m}}^{\mathrm{AF}}$.

Section 6. Correlation between the antiferromagnetic ordering and magnon diffusion length

To elucidate the correlation between the antiferromagnetic (AF) ordering and magnon diffusion length, we conduct numerical simulations for one-dimensional antiferromagnet layer with the atomistic Landau-Lifshitz-Gilbert equation (*52*). We consider the hard-axis anisotropy along the thickness direction and the easy-axis anisotropy in the plane for the NiO layer. Perfect AF ordering has the anti-parallel exchange coupling in alternating layers. We consider the AF ordering by changing the sign of the exchange coupling randomly. In other words, the amount of AF ordering means how many atoms have antiferromagnetic coupling in the whole sample. Therefore, AF ordering is defined as AF ordering (%) = (the number of atomic sites having the

antiferromagnetic exchange)/(total number of atomic sites)×100%. The magnon is excited at the bottom layer by an AC external field at 1.5 THz. Figure S5 shows the calculated magnon diffusion length $l_{\mathrm{m}}^{\mathrm{AF}}$ as a function of the antiferromagnetic ordering. We observe that the magnon diffusion length increases with increasing the antiferromagnetic ordering. This result suggests that there is a close correlation between the antiferromagnetic ordering and magnon diffusion length.

Section 7. Reproducible magnon-torque-driven magnetization switching in Bi_2Se_3/NiO/Py devices

The magnon-torque-driven magnetization switching is reproducible in other Bi_2Se_3 (8 nm)/NiO (25 nm)/Py (6 nm) devices, as shown in Fig. S6. We follow the same measurement procedures in Fig. 4 of the main text.

Section 8. Magnon-torque-driven magnetization switching in Bi_2Se_3/NiO/CoFeB devices

The magnon-torque-driven magnetization switching is also demonstrated in the Bi_2Se_3 (8 nm)/NiO (25 nm)/$Co_{40}Fe_{40}B_{20}$ (CoFeB, 3 nm) devices, as shown in Fig. S7. We follow the same measurement procedures used in Fig. 4 of the main text. The switching of CoFeB magnetization induced by magnon torques has an important implication for use in spintronic devices since CoFeB is widely used for magnetic tunnel junction (MTJ) and magnetoresistive random access memory (MRAM) applications.

Section 9. Reproducible magnon-torque-driven magnetization switching in Bi_2Se_3/NiO/Cu/Py devices

The magnon-torque-driven magnetization switching is reproducible in other Bi_2Se_3 (8 nm)/NiO (25 nm)/Cu (6 nm)/Py (6 nm) devices, as shown in Fig. S8. We follow the same measurement procedures in Fig. 4 of the main text.

Section 10. Estimation of the switching efficiency from switching experiments

We carry out switching experiments on Bi_2Se_3 (8 nm)/NiO (t_{NiO})/Py (6 nm) devices at various t_{NiO} ($\geq$ 2 nm). In these switching devices, the Py layer is also patterned into a rectangle so that the device structure is similar to that in Fig. 4. Figure S9A shows the switching current density J_C as a function of t_{NiO}. The switching is not observed for devices with t_{NiO} < 12.5 nm. Figure S9B shows the switching efficiency η as a function of t_{NiO}, where we define $\eta = H_P/J_C$ and H_P is the domain wall depinning field (*53*). We use this definition for the switching efficiency because the switching is governed by the domain nucleation and propagation in our device size. We find that η shows a qualitatively similar trend as θ_t in Fig. 3C of the main text.

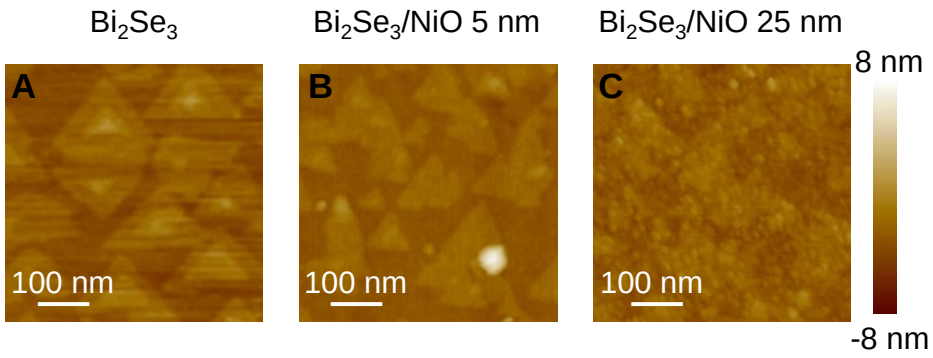

Fig. S1. Atomic-force microscopy (AFM) image of Bi_2Se_3 and Bi_2Se_3/NiO films. AFM images of anmolecular beam epitaxy (MBE) grown Bi_2Se_3 (8nm) (**A**), a Bi_2Se_3 (8nm)/NiO (5 nm) film (**B**), and a Bi_2Se_3 (8nm)/NiO (25 nm) film (**C**).

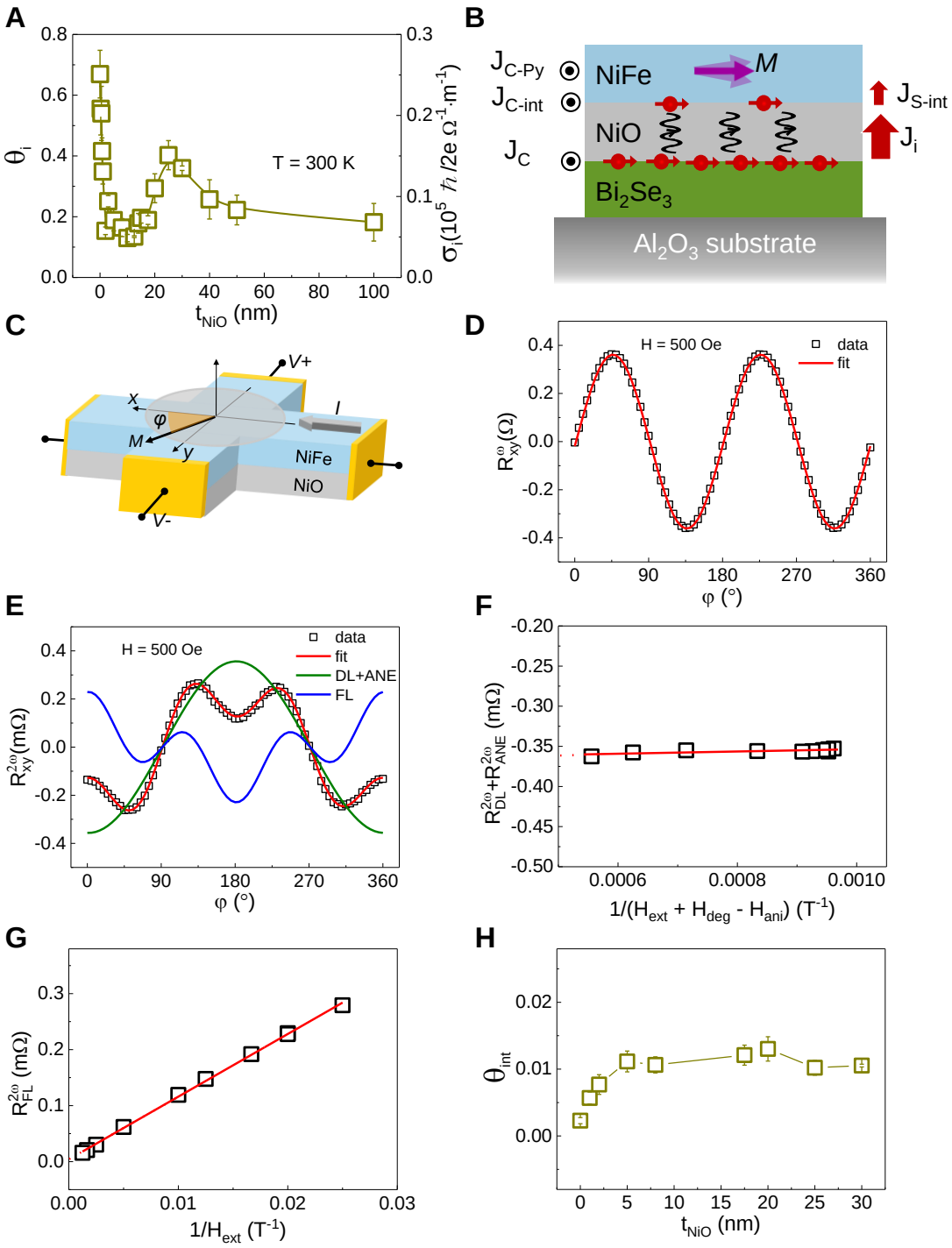

Fig. S2. Spin torque ratio θ_i and the NiO/Py interface contribution. (**A**) The t_{NiO} dependent spin torque ratio θ_i and spin conductivity σ_i from the symmetric component using ST-FMR measurements at room temperature. Here θ_i includes the contribution of the NiO/Py interface. (**B**) A cross section of the ST-FMR device along the I_{RF} direction. The red arrows with red balls and

the waved black wavy lines represent electron spins and magnon currents, respectively. (**C**) The schematic of the 1st and 2nd harmonic transverse voltage (or resistance) measurements. (**D**) R_{xy}^{ω} as a function of angle φ measured at H = 500 Oe and the fit. (**E**) $R_{xy}^{2\omega}$ as a function of angle φ measured at H = 500 Oe and the fit (red curve). The olive curve represents the 2nd harmonic transverse resistance $R_{DL}^{2\omega} + R_{ANE}^{2\omega}$ correlated with the damping-like torque τ_{DL} and anomalous Nernst effect, whereas the blue curve represents $R_{FL}^{2\omega}$ correlated with the field-like torque. (**F**) The summation of $R_{DL}^{2\omega}$ and $R_{ANE}^{2\omega}$ and (**G**) $R_{FL}^{2\omega}$ as a function of the static field experienced by the Py magnetization. (**H**) The electron spin torque θ_{int} at the NiO/Py interface as a function of NiO thickness at room temperature.

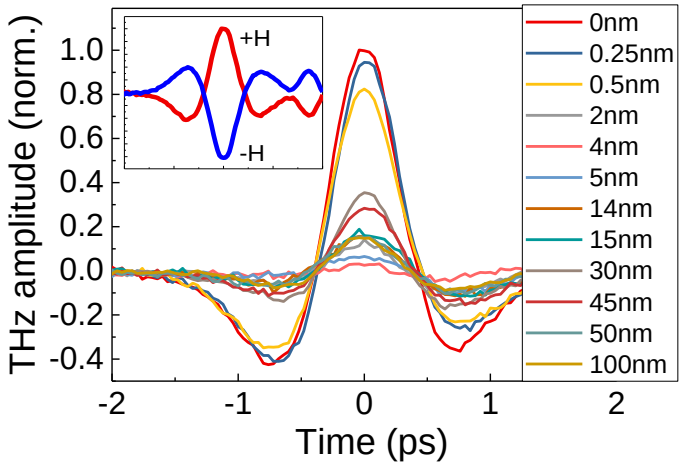

Fig. S3. Optical-driven THz emission in Bi_2Se_3/NiO (t_{NiO} = 0–100 nm)/Py films.

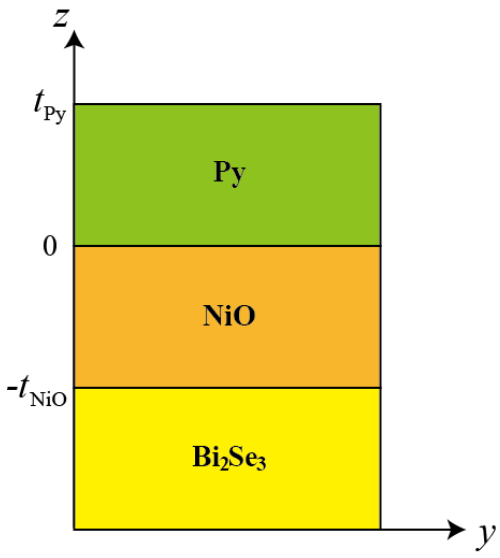

Fig. S4. Schematic illustration of the model system.

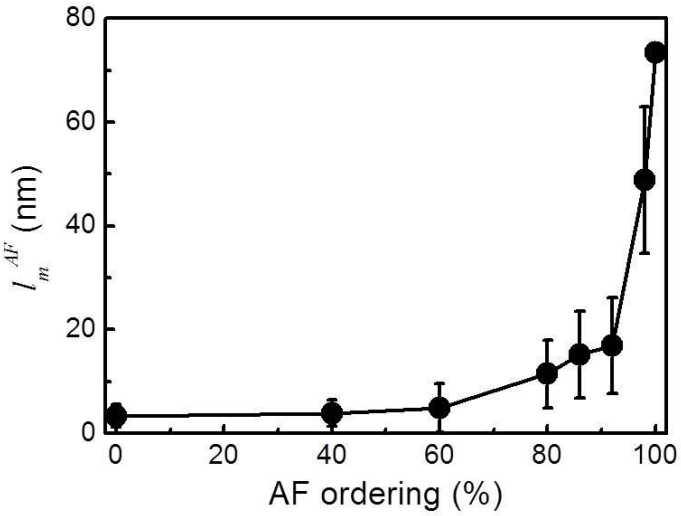

Fig. S5. The calculated magnon diffusion length l_m^{AF} as a function of the antiferromagnetic (AF) ordering. 100% represents a perfect antiferromagnet. The used parameters are damping constant = 0.005, exchange stiffness constant = -5×10^{-7} erg cm^{-1}, easy-axis anisotropy = 10^6 erg cm^{-3}, hard-axis anisotropy = -10^6 erg cm^{-3}, saturation magnetization = 800 emu cm^{-3}, and lattice constant = 0.4 nm.

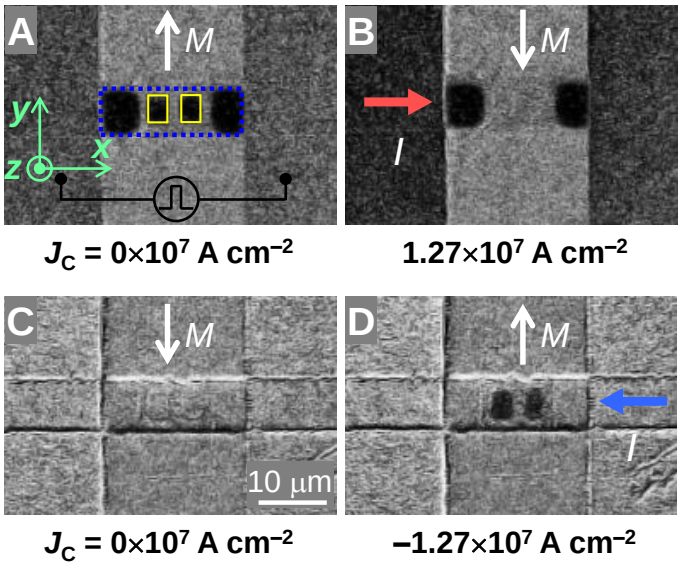

Fig. S6. Magnetization switching induced by magnon torque in the Bi_2Se_3/NiO/Py devices. MOKE images for the magnon-torque-driven magnetization switching using a pulsed current *I* along the +*x*-axis (**A**-**B**) and *I* along the –*x*-axis (**C**-**D**). The switching current density J_C is denoted underneath each image. The dark (light) contrast represents the magnetization along the +*y* (–*y*)-axis. The current channel is 8 μm wide denoted by the blue dashed box. The isolated Py rectangles are denoted by the yellow boxes with the magnetization direction indicated by the white arrow.

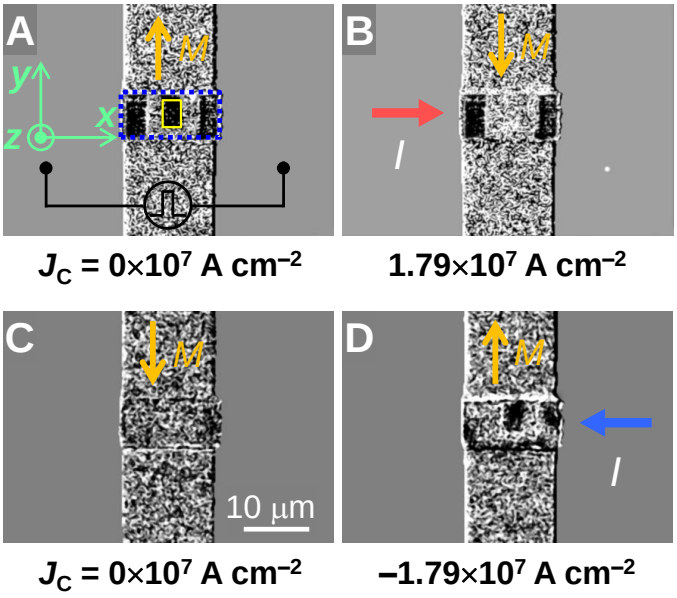

Fig. S7. Magnetization switching induced by magnon torque in the Bi_2Se_3/NiO/CoFeB devices. MOKE images for the magnon-torque-driven magnetization switching using a pulsed current *I* along the +*x*-axis (**A**-**B**) and *I* along the –*x*-axis (**C**-**D**). The switching current density J_C is denoted underneath each image. The dark (light) contrast represents the magnetization along the +*y* (–*y*)-axis. The current channel is 7 μm wide denoted by the blue dashed box. The isolated CoFeB rectangle is denoted by the yellow box with the magnetization direction indicated by the yellow arrow.

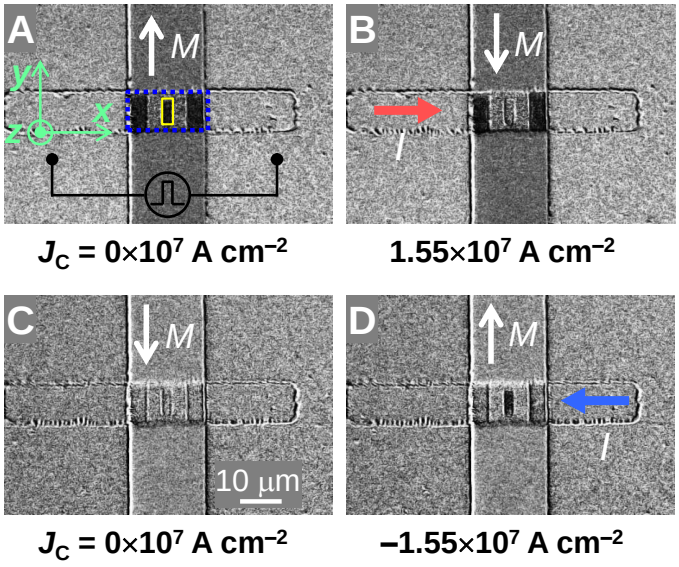

Fig. S8. Magnetization switching induced by magnon torque in the Bi_2Se_3/NiO/Cu/Py devices. MOKE images for the magnon-torque-driven magnetization switching using a pulsed current *I* along the +*x*-axis (**A**-**B**) and *I* along the –*x*-axis (**C**-**D**). The switching current density J_C is denoted underneath each image. The dark (light) contrast represents the magnetization along the +*y* (–*y*)-axis. The current channel is 9.5 μm wide denoted by the blue dashed box. The isolated Cu/Py bilayer rectangle is denoted by the yellow box with the magnetization direction indicated by the white arrow.

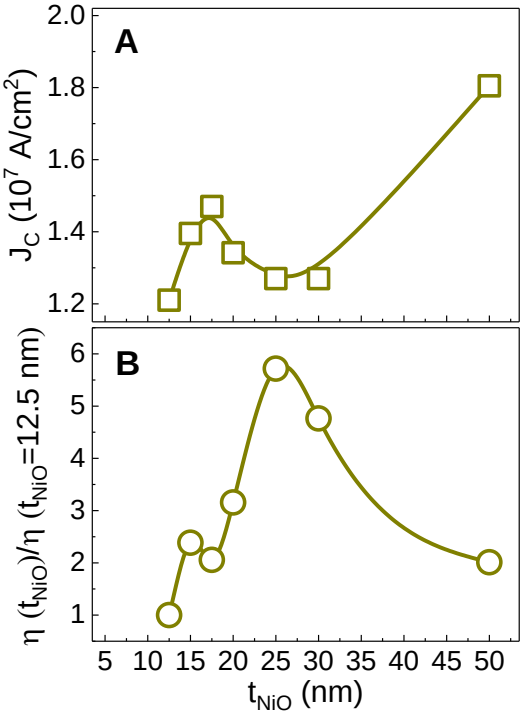

Fig. S9. The critical switching current density and switching efficiency from the magnetization switching measurements. (**A**) Switching current density J_C as a function of t_{NiO}. (**B**) Normalized switching efficiency as a function of t_{NiO}.

Table S1: Summary of control device structures and spin torque efficiencies

	Device structures (unit in nm)	θ_i^*	θ_i
C1	Sapphire sub./Bi_2Se_3 (8)/NiO (25)/**MgO (6)**/NiFe (6)	~0.09	~0.09
C2	Sapphire sub./Bi_2Se_3 (8)/**MgO (6)**/NiO (25) /NiFe (6)	~0.13	~0.03
D1	Sapphire sub./Bi_2Se_3 (8)/NiO (25)/NiFe (6)	~0.40	~0.30

θ_i (θ_i^*) represents the spin torque efficiency excluding (without excluding) the NiO/Py interface contribution.

References and Notes

1. J. C. Slonczewski, Current-driven excitation of magnetic multilayers. *J. Magn. Magn. Mater.* **159**, L1–L7 (1996). doi:10.1016/0304-8853(96)00062-5

2. L. Berger, Emission of spin waves by a magnetic multilayer traversed by a current. *Phys. Rev. B* **54**, 9353–9358 (1996). doi:10.1103/PhysRevB.54.9353 Medline

3. A. Brataas, A. D. Kent, H. Ohno, Current-induced torques in magnetic materials. *Nat. Mater.* **11**, 372–381 (2012). doi:10.1038/nmat3311 Medline

4. J. Bass, W. P. Pratt Jr., Spin-diffusion lengths in metals and alloys, and spin-flipping at metal/metal interfaces: An experimentalist's critical review. *J. Phys. Condens. Matter* **19**, 183201 (2007). doi:10.1088/0953-8984/19/18/183201

5. A. Chumak, V. Vasyuchka, A. Serga, B. Hillebrands, Magnon spintronics. *Nat. Phys.* **11**, 453–461 (2015). doi:10.1038/nphys3347

6. Y. Kajiwara, K. Harii, S. Takahashi, J. Ohe, K. Uchida, M. Mizuguchi, H. Umezawa, H. Kawai, K. Ando, K. Takanashi, S. Maekawa, E. Saitoh, Transmission of electrical signals by spin-wave interconversion in a magnetic insulator. *Nature* **464**, 262–266 (2010). doi:10.1038/nature08876 Medline

7. L. Cornelissen, J. Liu, R. Duine, J. B. Youssef, B. Van Wees, Long-distance transport of magnon spin information in a magnetic insulator at room temperature. *Nat. Phys.* **11**, 1022–1026 (2015). doi:10.1038/nphys3465

8. W. Yuan, Q. Zhu, T. Su, Y. Yao, W. Xing, Y. Chen, Y. Ma, X. Lin, J. Shi, R. Shindou, X. C. Xie, W. Han, Experimental signatures of spin superfluid ground state in canted antiferromagnet Cr_2O_3 via nonlocal spin transport. *Sci. Adv.* **4**, eaat1098 (2018). doi:10.1126/sciadv.aat1098 Medline

9. R. Lebrun, A. Ross, S. A. Bender, A. Qaiumzadeh, L. Baldrati, J. Cramer, A. Brataas, R. A. Duine, M. Kläui, Tunable long-distance spin transport in a crystalline antiferromagnetic iron oxide. *Nature* **561**, 222–225 (2018). doi:10.1038/s41586-018-0490-7 Medline

10. J. C. Slonczewski, Initiation of spin-transfer torque by thermal transport from magnons. *Phys. Rev. B* **82**, 054403 (2010). doi:10.1103/PhysRevB.82.054403

11. P. Yan, X. S. Wang, X. R. Wang, All-magnonic spin-transfer torque and domain wall propagation. *Phys. Rev. Lett.* **107**, 177207 (2011). doi:10.1103/PhysRevLett.107.177207 Medline

12. D. Hinzke, U. Nowak, Domain wall motion by the magnonic spin Seebeck effect. *Phys. Rev. Lett.* **107**, 027205 (2011). doi:10.1103/PhysRevLett.107.027205 Medline

13. A. A. Kovalev, Y. Tserkovnyak, Thermomagnonic spin transfer and Peltier effects in insulating magnets. *EPL* **97**, 67002 (2012) (Europhysics Letters). doi:10.1209/0295-5075/97/67002

14. W. Jiang, P. Upadhyaya, Y. Fan, J. Zhao, M. Wang, L.-T. Chang, M. Lang, K. L. Wong, M. Lewis, Y.-T. Lin, J. Tang, S. Cherepov, X. Zhou, Y. Tserkovnyak, R. N. Schwartz, K. L. Wang, Direct imaging of thermally driven domain wall motion in magnetic insulators. *Phys. Rev. Lett.* **110**, 177202 (2013). doi:10.1103/PhysRevLett.110.177202 Medline

15. T. Moriyama, S. Takei, M. Nagata, Y. Yoshimura, N. Matsuzaki, T. Terashima, Y. Tserkovnyak, T. Ono, Anti-damping spin transfer torque through epitaxial nickel oxide. *Appl. Phys. Lett.* **106**, 162406 (2015). doi:10.1063/1.4918990

16. S. Woo, T. Delaney, G. S. Beach, Magnetic domain wall depinning assisted by spin wave bursts. *Nat. Phys.* **13**, 448–454 (2017). doi:10.1038/nphys4022

17. A. R. Mellnik, J. S. Lee, A. Richardella, J. L. Grab, P. J. Mintun, M. H. Fischer, A. Vaezi, A. Manchon, E.-A. Kim, N. Samarth, D. C. Ralph, Spin-transfer torque generated by a topological insulator. *Nature* **511**, 449–451 (2014). doi:10.1038/nature13534 Medline

18. Y. Wang, D. Zhu, Y. Wu, Y. Yang, J. Yu, R. Ramaswamy, R. Mishra, S. Shi, M. Elyasi, K.-L. Teo, Y. Wu, H. Yang, Room temperature magnetization switching in topological insulator-ferromagnet heterostructures by spin-orbit torques. *Nat. Commun.* **8**, 1364 (2017). doi:10.1038/s41467-017-01583-4 Medline

19. J. Han, A. Richardella, S. A. Siddiqui, J. Finley, N. Samarth, L. Liu, Room-temperature spin-orbit torque switching induced by a topological insulator. *Phys. Rev. Lett.* **119**, 077702 (2017). doi:10.1103/PhysRevLett.119.077702 Medline

20. Materials and methods are available as supplementary materials.

21. C. Hahn, G. de Loubens, V. V. Naletov, J. Ben Youssef, O. Klein, M. Viret, Conduction of spin currents through insulating antiferromagnetic oxides. *EPL* **108**, 57005 (2014) (Europhysics Letters). doi:10.1209/0295-5075/108/57005

22. H. Wang, C. Du, P. C. Hammel, F. Yang, Antiferromagnonic spin transport from $Y_3Fe_5O_{12}$ into NiO. *Phys. Rev. Lett.* **113**, 097202 (2014). doi:10.1103/PhysRevLett.113.097202 Medline

23. W. Lin, K. Chen, S. Zhang, C. L. Chien, Enhancement of thermally injected spin current through an antiferromagnetic insulator. *Phys. Rev. Lett.* **116**, 186601 (2016). doi:10.1103/PhysRevLett.116.186601 Medline

24. D. Hou, Z. Qiu, J. Barker, K. Sato, K. Yamamoto, S. Vélez, J. M. Gomez-Perez, L. E. Hueso, F. Casanova, E. Saitoh, Tunable sign change of spin Hall magnetoresistance in Pt/NiO/YIG structures. *Phys. Rev. Lett.* **118**, 147202 (2017). doi:10.1103/PhysRevLett.118.147202 Medline

25. S. Rezende, R. Rodríguez-Suárez, A. Azevedo, Diffusive magnonic spin transport in antiferromagnetic insulators. *Phys. Rev. B* **93**, 054412 (2016). doi:10.1103/PhysRevB.93.054412

26. J. Nogués, I. K. Schuller, Exchange bias. *J. Magn. Magn. Mater.* **192**, 203–232 (1999). doi:10.1016/S0304-8853(98)00266-2

27. Y. Wang, P. Deorani, K. Banerjee, N. Koirala, M. Brahlek, S. Oh, H. Yang, Topological surface states originated spin-orbit torques in Bi_2Se_3. *Phys. Rev. Lett.* **114**, 257202 (2015). doi:10.1103/PhysRevLett.114.257202 Medline

28. Y. Wang, R. Ramaswamy, H. Yang, FMR-related phenomena in spintronic devices. *J. Phys. D Appl. Phys.* **51**, 273002 (2018). doi:10.1088/1361-6463/aac7b5

29. S. S.-L. Zhang, S. Zhang, Spin convertance at magnetic interfaces. *Phys. Rev. B* **86**, 214424 (2012). doi:10.1103/PhysRevB.86.214424

30. A. Hoffmann, Spin Hall effects in metals. *IEEE Trans. Magn.* **49**, 5172–5193 (2013). doi:10.1109/TMAG.2013.2262947

31. Y. Wu, M. Elyasi, X. Qiu, M. Chen, Y. Liu, L. Ke, H. Yang, High-Performance THz Emitters Based on Ferromagnetic/Nonmagnetic Heterostructures. *Adv. Mater.* **29**, 1603031 (2017). doi:10.1002/adma.201603031 Medline

32. L. Cheng, X. Wang, W. Yang, J. Chai, M. Yang, M. Chen, Y. Wu, X. Chen, D. Chi, K. E. J. Goh, J.-X. Zhu, H. Sun, S. Wang, J. C. W. Song, M. Battiato, H. Yang, E. E. M. Chia, Far out-of-equilibrium spin populations trigger giant spin injection into atomically thin MoS_2. *Nat. Phys.* **15**, 347–351 (2019). doi:10.1038/s41567-018-0406-3

33. O. Mosendz, J. Pearson, F. Fradin, S. Bader, A. Hoffmann, Suppression of spin-pumping by a MgO tunnel-barrier. *Appl. Phys. Lett.* **96**, 022502 (2010). doi:10.1063/1.3280378

34. Z. Qiu, J. Li, D. Hou, E. Arenholz, A. T. N'Diaye, A. Tan, K. Uchida, K. Sato, S. Okamoto, Y. Tserkovnyak, Z. Q. Qiu, E. Saitoh, Spin-current probe for phase transition in an insulator. *Nat. Commun.* **7**, 12670 (2016). doi:10.1038/ncomms12670 Medline

35. A. Prakash, J. Brangham, F. Yang, J. P. Heremans, Spin Seebeck effect through antiferromagnetic NiO. *Phys. Rev. B* **94**, 014427 (2016). doi:10.1103/PhysRevB.94.014427

36. Y. Cheng, K. Chen, S. Zhang, Giant magneto-spin-Seebeck effect and magnon transfer torques in insulating spin valves. *Appl. Phys. Lett.* **112**, 052405 (2018). doi:10.1063/1.5018411

37. A. Brataas, Y. V. Nazarov, G. E. Bauer, Finite-element theory of transport in ferromagnet-normal metal systems. *Phys. Rev. Lett.* **84**, 2481–2484 (2000). doi:10.1103/PhysRevLett.84.2481 Medline

38. T. Ikebuchi, T. Moriyama, H. Mizuno, K. Oda, T. Ono, Spin current transmission in polycrystalline NiO films. *Appl. Phys. Express* **11**, 073003 (2018). doi:10.7567/APEX.11.073003

39. C. Y. Guo, C. H. Wan, X. Wang, C. Fang, P. Tang, W. J. Kong, M. K. Zhao, L. N. Jiang, B. S. Tao, G. Q. Yu, X. F. Han, Magnon valves based on YIG/NiO/YIG all-insulating magnon junctions. *Phys. Rev. B* **98**, 134426 (2018). doi:10.1103/PhysRevB.98.134426

40. Y. Wang *et al*., Replication Data and Code for: Magnetization switching by magnon-mediated spin torque through an antiferromagnetic insulator, Harvard Dataverse (2019); doi:10.7910/DVN/OCWIDN

41. H. An, Y. Kageyama, Y. Kanno, N. Enishi, K. Ando, Spin-torque generator engineered by natural oxidation of Cu. *Nat. Commun.* **7**, 13069 (2016). doi:10.1038/ncomms13069 Medline

42. K.-U. Demasius, T. Phung, W. Zhang, B. P. Hughes, S.-H. Yang, A. Kellock, W. Han, A. Pushp, S. S. P. Parkin, Enhanced spin-orbit torques by oxygen incorporation in tungsten films. *Nat. Commun.* **7**, 10644 (2016). doi:10.1038/ncomms10644 Medline

43. H. An, T. Ohno, Y. Kanno, Y. Kageyama, Y. Monnai, H. Maki, J. Shi, K. Ando, Current-induced magnetization switching using an electrically insulating spin-torque generator. *Sci. Adv.* **4**, eaar2250 (2018). doi:10.1126/sciadv.aar2250 Medline

44. C. O. Avci, K. Garello, M. Gabureac, A. Ghosh, A. Fuhrer, S. F. Alvarado, P. Gambardella, Interplay of spin-orbit torque and thermoelectric effects in ferromagnet/normal-metal bilayers. *Phys. Rev. B Condens. Matter Mater. Phys.* **90**, 224427 (2014). doi:10.1103/PhysRevB.90.224427

45. Y. Wen, J. Wu, P. Li, Q. Zhang, Y. Zhao, A. Manchon, J. Q. Xiao, X. Zhang, Temperature dependence of spin-orbit torques in Cu-Au alloys. *Phys. Rev. B* **95**, 104403 (2017). doi:10.1103/PhysRevB.95.104403

46. Q. Shao, G. Yu, Y.-W. Lan, Y. Shi, M.-Y. Li, C. Zheng, X. Zhu, L.-J. Li, P. K. Amiri, K. L. Wang, Strong Rashba-Edelstein effect-induced spin-orbit torques in monolayer transition metal dichalcogenide/ferromagnet bilayers. *Nano Lett.* **16**, 7514–7520 (2016). doi:10.1021/acs.nanolett.6b03300 Medline

47. Y. Wang, P. Deorani, X. Qiu, J. H. Kwon, H. Yang, Determination of intrinsic spin Hall angle in Pt. *Appl. Phys. Lett.* **105**, 152412 (2014). doi:10.1063/1.4898593

48. T. Kampfrath, M. Battiato, P. Maldonado, G. Eilers, J. Nötzold, S. Mährlein, V. Zbarsky, F. Freimuth, Y. Mokrousov, S. Blügel, M. Wolf, I. Radu, P. M. Oppeneer, M. Münzenberg, Terahertz spin current pulses controlled by magnetic heterostructures. *Nat. Nanotechnol.* **8**, 256–260 (2013). doi:10.1038/nnano.2013.43 Medline

49. T. J. Huisman, R. V. Mikhaylovskiy, J. D. Costa, F. Freimuth, E. Paz, J. Ventura, P. P. Freitas, S. Blügel, Y. Mokrousov, T. Rasing, A. V. Kimel, Femtosecond control of electric currents in metallic ferromagnetic heterostructures. *Nat. Nanotechnol.* **11**, 455–458 (2016). doi:10.1038/nnano.2015.331 Medline

50. M. Chen, R. Mishra, Y. Wu, K. Lee, H. Yang, Terahertz emission from compensated magnetic heterostructures. *Adv. Opt. Mater.* **6**, 1800430 (2018). doi:10.1002/adom.201800430

51. K. Lee, J. Li, L. Cheng, J. Wang, D. Kumar, Q. Wang, M. Chen, Y. Wu, G. Eda, E. E. M. Chia, H. Chang, H. Yang, Sub-picosecond carrier dynamics induced by efficient charge transfer in $MoTe_2/WTe_2$ van der Waals heterostructures. *ACS Nano* **13**, 9587–9594 (2019). doi:10.1021/acsnano.9b04701 Medline

52. T. Shiino, S.-H. Oh, P. M. Haney, S.-W. Lee, G. Go, B.-G. Park, K.-J. Lee, Antiferromagnetic domain wall motion driven by spin-orbit torques. *Phys. Rev. Lett.* **117**, 087203 (2016). doi:10.1103/PhysRevLett.117.087203 Medline

53. R. Mishra, J. Yu, X. Qiu, M. Motapothula, T. Venkatesan, H. Yang, Anomalous current-induced spin torques in ferrimagnets near compensation. *Phys. Rev. Lett.* **118**, 167201 (2017). doi:10.1103/PhysRevLett.118.167201 Medline